A numerical simulation of the μ^+SR experiment

Tom Lancaster and Stephen J Blundell
Clarendon Laboratory,
Oxford University Department of Physics,
Parks Road, Oxford, OX1 3PU, UK

December 11, 2004

In this paper we present the results of numerical simulations of the μ^+SR experiment as realised on three spectrometers. Our interest here is in the relativistic dynamics of the particles involved in the experiment. We begin with considering the magnetic fields applied to the sample before deriving their effect on charged particles. The effect of the fields on the incoming muon beam and outgoing positron ensemble are considered before results are presented on the existing EMU and ALC spectrometers and on a proposed geometry for a new spectrometer. Preliminary results from the simulations have been published as indicated in reference [1].

1 Introduction

The application of external magnetic fields to the sample is of considerable importance in a μ^+SR experiment. Currently, the maximum available field at ISIS is 0.45 T, while at PSI it is 3 T. In recent months there has been an effort in both facilities to investigate the possibility of building new instruments where higher magnetic fields are attainable.

High magnetic fields would present a number of opportunities for muon science. In magnetic materials, the range of fluctuation rates that could be probed would be increased. For molecular materials, where there is the possibility of muonium radicals, higher fields would enable both the separation of static and dynamic relaxation and the investigation of hyperfine fields via avoided level crossing resonances. The range of mechanisms for the diffusion of light particles which can be probed by the experiment would also be extended. High fields are also useful for quenching unwanted relaxation mechanisms such as that due to muonium spin-exchange effects [1].

1.1 The need for the simulation of instruments

The possibility of high magnetic fields being applied to a μ^+SR experiment presents considerable complications. The experiment relies on the motion of

charged particles. The application of a magnetic field B will cause the particles to experience a Lorentz force, which will modify its motion.

The incoming positive muons travel from the production target to the sample environment, where they are implanted in the sample. The modification of the motion of the muon caused by an applied field may cause a change in the illumination of the sample by the muon beam, either by focusing or defocussing the beam or, in extreme cases, by causing muons to miss the sample completely.

Outgoing positrons, from which the information on the polarization of the stopped muon ensemble is extracted, travel from the sample position to the detector arrays. In most current applications, where the applied fields are small, we assume rectilinear motion from the sample to the detectors. An applied field in this case may cause the positron to impinge on a different detector to that expected or to miss the detector array completely.

It is clearly necessary, therefore, to come to a detailed understanding of the mechanics of the particles involved in the experiment. This understanding must then be applied to existing experimental geometries and to the designs of new instruments with more complex, or extreme environments. We present here the methodology and results of a numerical simulation of the μ^+SR experiment.

2 Theoretical considerations

2.1 External magnetic fields

The applied magnetic fields in a μ^+SR experiment are achieved by passing current through a network. The network may, mathematically, be described as formed from the sum of many current carrying elements $I\mathrm{d}\mathbf{l}$. An element $I\mathrm{d}\mathbf{l}$ at a position $\mathbf{x}'$ will give rise to an infinitesimal magnetic field $\mathrm{d}\mathbf{B}$ at a position $\mathbf{x}$ given by the Biot-Savart law [2]

$$\mathrm{d}\mathbf{B}(\mathbf{x}) = \frac{\mu_0 I\mathrm{d}\mathbf{l} \times (\mathbf{x} - \mathbf{x}')}{4\pi|\mathbf{x} - \mathbf{x}'|^3}, \tag{1}$$

where μ_0 is the permeability of free space. A knowledge of the geometry of the current network, therefore, allows the calculation of the magnetic fields in the environment of the experiment.

2.2 Relativistic particle mechanics

The positrons that emerge from muon decay have energies ξ up to $\xi_{\mathrm{max}} = 52.83$ MeV. This corresponds to a velocity $v = 0.9999c$. It is clear, therefore, that the results of classical mechanics will not be valid and use must be made of the results from special relativity. In this section we discuss the relevant results from the classical theory of fields. Tensor notation is used freely from the outset and the Einstein summation convention is assumed [3].

2.2.1 The equations of motion

We define the contravariant four-vector for position by

$$x^i = (ct, \mathbf{x}), \tag{2}$$

where $\mathbf{x}$ is the position three vector, t is the time coordinate and c is the speed of light.

The Lorentz transformations, for a frame moving with velocity v, may then be written as

$$x^\mu = \Lambda^\mu_{\ \nu} x^\nu, \tag{3}$$

where

$$\Lambda^\mu_{\ \nu} = \begin{pmatrix} \gamma & -\beta\gamma & 0 & 0 \\ -\beta\gamma & \gamma & 0 & 0 \\ 0 & 0 & 1 & 0 \\ 0 & 0 & 0 & 1 \end{pmatrix}, \tag{4}$$

where $\beta = v/c$ and

$$\gamma = \left(1 - \frac{v^2}{c^2}\right)^{-\frac{1}{2}}. \tag{5}$$

The raising and lowering of indices is achieved through the application of the Minkovski metric tensor:

$$g^{ik} = g_{ik} = \begin{pmatrix} -1 & 0 & 0 & 0 \\ 0 & 1 & 0 & 0 \\ 0 & 0 & 1 & 0 \\ 0 & 0 & 0 & 1 \end{pmatrix}. \tag{6}$$

Using equation (6), we may evaluate the invariant $\mathrm{d}s$, defined by

$$\mathrm{d}s^2 = \mathrm{d}x^i \mathrm{d}x_i. \tag{7}$$

yielding, for an inertial frame S,

$$\mathrm{d}s^2 = -c^2 \mathrm{d}t^2 + \mathrm{d}x^2 + \mathrm{d}y^2 + \mathrm{d}z^2. \tag{8}$$

We may equate this expression for the invariant quantity $\mathrm{d}s^2$, with that obtained for a particle at rest in a system of coordinates S', (i.e. $\mathrm{d}x' + \mathrm{d}y' + \mathrm{d}z' = 0$), yielding

$$\mathrm{d}t' = \mathrm{d}t \left(1 - \frac{\mathrm{d}x^2 + \mathrm{d}y^2 + \mathrm{d}z^2}{c^2 \mathrm{d}t^2}\right)^{\frac{1}{2}}, \tag{9}$$

and thus

$$\mathrm{d}t' = \mathrm{d}t \left(1 - \frac{v^2}{c^2}\right)^{\frac{1}{2}} = \frac{\mathrm{d}s}{c}, \tag{10}$$

which defines the proper time interval $\mathrm{d}\tau = \mathrm{d}t' = \mathrm{d}t/\gamma$.

We also define the (dimensionless) four-velocity of a particle

$$u^i = \frac{\mathrm{d}x^i}{\mathrm{d}s}. \tag{11}$$

The components of this vector may be evaluated using equation (10), yielding the result

$$u^i = \gamma\left(1, \frac{\mathbf{v}}{c}\right), \tag{12}$$

where $\mathbf{v}$ is the ordinary three-velocity.

We are now in a position to consider the equations of motion of a relativistic particle in electric and magnetic fields. The $\mathbf{E}$ and $\mathbf{B}$ fields transform as

$$F^{ik} = \Lambda^i{}_\mu \Lambda^k{}_\nu F^{\mu\nu}, \tag{13}$$

where F^{ik} is the Maxwell field tensor

$$F^{ik} = \begin{pmatrix} 0 & -E_x/c & -E_y/c & -E_z/c \\ E_x/c & 0 & -B_z & B_y \\ E_y/c & B_z & 0 & -B_x \\ E_z/c & -B_y & B_x & 0 \end{pmatrix}. \tag{14}$$

The equations of motion may be derived through considering the relativistic Lagrangian [3], which yields

$$mc\frac{\mathrm{d}u^i}{\mathrm{d}s} = qF^{ik}u_k. \tag{15}$$

Substituting for u^i from equation (11) gives the equation of motion for a particle with three velocity $\mathbf{v}$:

$$\frac{\mathrm{d}}{\mathrm{d}t}(m\gamma\mathbf{v}) = q(\mathbf{E} + \mathbf{v} \times \mathbf{B}). \tag{16}$$

2.3 Radiation from accelerating charges

It is well known that an accelerating charge will emit electromagnetic radiation. In this section we consider the energy lost by a particle and the resulting modifications to the equation of motion in both the non-relativistic ($|\mathbf{v}| \ll c$, $\gamma \approx 1$) and ultra relativistic ($|\mathbf{v}| \sim c$, $\gamma \gg 1$) limits.

2.3.1 Dipole radiation

We begin by considering the non-relativistic case of a fluctuating charge distribution. We describe this distribution in terms of a current density four-vector

$$j^\mu = j(t, \mathbf{x}) = q\frac{\mathrm{d}x^\mu}{\mathrm{d}\tau}. \tag{17}$$

The required quantity is the retarded four-vector potential. A system of charges at positions $\mathbf{x}'$, gives rise to a field A^μ at $(t, \mathbf{x})$ given by [3]

$$A^\mu = A(t, \mathbf{x}) = \frac{\mu_0}{4\pi} \int \frac{j(t - |\mathbf{x} - \mathbf{x}'|/c, \mathbf{x}')}{|\mathbf{x} - \mathbf{x}'|} \mathrm{d}^3\mathbf{x}'. \tag{18}$$

The spacial components of this vector at large distances $|\mathbf{x} - \mathbf{x}'|$ are well approximated by the vector potential

$$\mathbf{A}(t, \mathbf{x}) = \frac{\mu_0}{4\pi|\mathbf{x}|} \left. \frac{\mathrm{d}\mathbf{p}}{\mathrm{d}t} \right|_{(t-|\mathbf{x}|/c)}, \tag{19}$$

where $\mathbf{p} = \sum q\mathbf{x}'$ is the dipole moment of the charges.

The radiated power P may be evaluated using standard methods [3] yielding Larmor's formula:

$$P = \frac{\mu_0 |\ddot{\mathbf{p}}|^2}{6\pi c}. \tag{20}$$

For a single charge q we obtain

$$P = \frac{q^2}{4\pi\epsilon_0} \frac{2|\dot{\mathbf{v}}|^2}{3c^3}. \tag{21}$$

or, in terms of the energy change $\mathrm{d}\xi$

$$\mathrm{d}\xi = \frac{q^2}{4\pi\epsilon_0} \frac{2|\dot{\mathbf{v}}|^2}{3c^3} \mathrm{d}t. \tag{22}$$

2.3.2   Radiation from rapidly moving charges

The discussion above may be generalised to the case of a relativistic particle. In a frame of reference where the particle is at rest the amount of energy radiated in the time interval $\mathrm{d}t$ is given by equation (22). In this frame of reference, the total radiated momentum is zero.

Equation (22) may be written in four-dimensional form

$$\mathrm{d}P^i = -\frac{q^2}{4\pi\epsilon_0} \frac{2}{3c^3} \frac{\mathrm{d}u^k}{\mathrm{d}s} \frac{\mathrm{d}u_k}{\mathrm{d}s} u^i \mathrm{d}s. \tag{23}$$

The total radiated four momentum is then given by

$$\Delta P^i = -\frac{q^2}{4\pi\epsilon_0} \frac{2}{3m^2c^5} \int (F_{kl}u^l)(F^{kl}u_m)\mathrm{d}x^i, \tag{24}$$

while the radiated energy is found by evaluating the time component of equation (24)

$$\Delta\xi = \frac{q^2}{4\pi\epsilon_0} \frac{2}{3c^3} \int_{-\infty}^{\infty} \frac{|\dot{\mathbf{v}}|^2 - \frac{(\mathbf{v}\times\dot{\mathbf{v}})^2}{c^2}}{(1 - \frac{v^2}{c^2})^2} \mathrm{d}t. \tag{25}$$

2.3.3   Radiation damping

We must consider the modification to the equations of motion due to the radiation effects described above. A formal treatment of radiation damping requires the modification of the Lagrangian via the expansion of potentials to third (or possibly higher) orders. This approached may be found in reference [3].

It can be shown, for non-relativistic particles, that the average work done by the field is equal to the average energy radiated in unit time:

$$\overline{\mathbf{f} \cdot \mathbf{v}} = \frac{\mu_0}{6\pi c^3} \overline{\ddot{\mathbf{p}}^2} = \frac{q^2}{4\pi\epsilon_0} \frac{\overline{2|\dot{\mathbf{v}}|^2}}{3c^3}, \tag{26}$$

from which it follows that the three-force on a particle due to the emission of radiation is, in the limit of small velocities, given by

$$\mathbf{f} = \frac{q^2}{4\pi\epsilon_0} \frac{2}{3c^3} \dddot{\mathbf{v}}. \tag{27}$$

In the relativistic case, we require a four-vector force g^i, such that the equations of motion will take on the covariant form

$$mc\frac{\mathrm{d}u^i}{\mathrm{d}s} = qF^{ik}u_k + g^i. \tag{28}$$

A suitable four-vector is

$$g^i = \frac{q^2}{4\pi\epsilon_0} \frac{2}{3c^3} \left(\frac{\mathrm{d}^2 u^i}{\mathrm{d}s^2} - u^i u^k \frac{\mathrm{d}^2 u_k}{\mathrm{d}s^2} . \right) \tag{29}$$

For the ultra-relativistic case, the three-force becomes

$$\mathbf{f} = \frac{q^4}{4\pi\epsilon_0} \frac{2}{3m^2c^5} (F_{kl}u^l)(F^{km}u_m)\mathbf{n}, \tag{30}$$

where $\mathbf{n}$ is a unit vector along the direction of $\mathbf{v}$. Evaluating this explicitly for motion in the x-direction yields the result

$$f_x = -\frac{q^4}{4\pi\epsilon_0} \frac{2}{3m^2c^5} \frac{(E_y/c - B_z)^2 + (E_z/c + B_y)^2}{1 - \frac{v^2}{c^2}}, \tag{31}$$

which shows that the force acts in a direction opposite to that of the particle's velocity. We note also that the radiation damping is proportional to the square of the particle's energy.

3 A numerical simulation

A numerical simulation of the μ^+SR experiment has been carried out employing the theoretical results above. The results of the simulation are computed using a program written in FORTRAN.

The muon beam is injected at $z = -1$ m, with velocity in the positive z-direction. The sample is located at $z = 0$ such that it is assumed that all muons will stop in in the $z = 0$ plane. The muons retain their polarization (along $-z$) in the stopping process. A physical realisation of this picture would be a silver plate, with a large area located at the sample position.
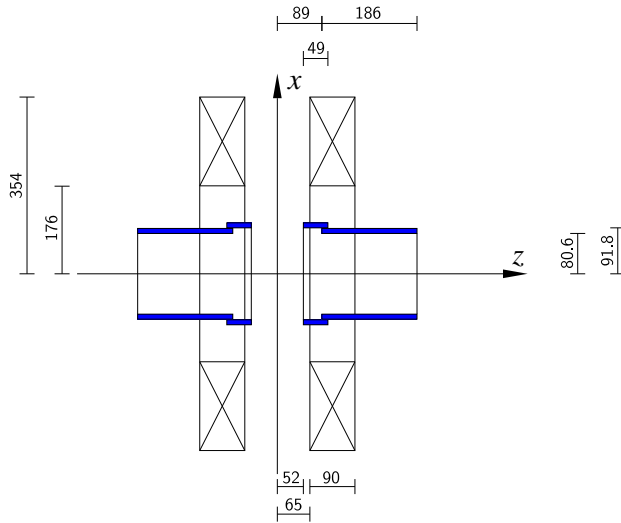
Figure 1: Schematic cross-section of the EMU spectrometer showing the Helmholtz coils and detector arrays. The detector arrays are shown in blue. The sample is located at the origin. All measurements are in millimetres.

Initially, the geometry modelled was that of the EMU spectrometer [5] as shown in figure 1. The magnetic field is created by a pair of Helmholtz coils, whose dimensions are shown in the figure. The detector array and Helmholtz coils have cylindrical symmetry, making radial directions within the x-y plane equivalent, which simplifies the calculation. The magnetic fields were calculated using equation (1) for a cubic array of 500^3 points, corresponding to a real space volume of 5 m^3. The integration was carried out using an algorithm based on Simpson's rule [4] while the field between grid-points was determined by a simple interpolation.

The design of the Helmholtz coils is intended to supply an homogeneous field in the z-direction. The general tendency of charges in a uniform field is to execute cyclotron motion [3]. The trajectory of a charge q will be helical, with a radius r given by

$$r = |\mathbf{v}_\mathrm{T}|\xi/qBc^2, \tag{32}$$

where $|\mathbf{v}_\mathrm{T}|$ is the magnitude of the component of velocity in the x-y plane and ξ is the positron energy.

The problem of modelling the μ^+SR experiment splits into three parts: The motion of the incoming muon beam, the paths of the decay positrons and the detection of those positrons in in instrument's detector arrays. We examine each in turn.

7

3.1 The incoming muon beam

The principles at work are well illustrated with the simple case of a collimated muon beam with a square cross section of area 1 cm^2. We remove the sample and simply track the trajectories of positron beams located at the corners of the square beam profile. Results of this procedure are shown in figure 2 for an applied field of 0.45 T (the maximum field currently available on EMU).

We see that even at these relatively low fields the muon paths are perturbed by the presence of the field. In the case shown the field is seen to focus down the muon beam for $z > 0.4$ m. The focusing effect will, at higher fields, cause the beam spot size at the sample to vary with applied field. This effect is illustrated in figure 3 for a beam with a circular cross section (with an initial radius of 1 cm). We see that the radius of the circular beam profile at the sample, varies in a roughly periodic fashion with applied field.

3.2 The outgoing positrons

The outgoing positrons will clearly be affected far more dramatically by the applied field due to their smaller mass and larger initial velocities. The effects may be illustrated by considering a simple positron ensemble. We consider eight paths in the x-z plane, equally spaced in angle θ to the z axis. All positrons are given the maximum allowable energy ξ_{max}.

Figure 4 shows the results of the calculation for two applied fields. When $B = 0.45$ T (figure 4(a)), the paths are not significantly perturbed by the B-field when compared to the radius of the cylindrical detector arrays. In contrast, an applied field of 3 T causes a significant change in the trajectories of the outgoing positrons. It can be readily imagined that a particle under the influence of this field may have its path perturbed enough to miss the detector on which it would have impinged, had the field not been applied.

3.3 The instrument simulation

Using the results of the previous sections allows a full simulation of the μ^+SR experiment using EMU. Making the calculation tractable for a desktop PC inevitably results in a number of approximations.

We model a pulse of 1000 muons with zero pulse width. This pulse begins at $z = -1$ m with muons distributed normally within a rectangular beam with a cross-section of 30 mm$\times$15 mm. The muons stop at $z = 0$, where their coordinates x^μ are recorded. A Monte-Carlo approach is used to model the muon decay [4]. The emitted positron has its energy ξ and angle θ to the z axis chosen according to the known distributions. The positron path is then calculated.

The positron is detected by the instrument when it impinges on a scintillation detector. The detector geometry for EMU is shown in figure 1. Two pairs of detector arrays are employed, each arranged into a pair of cylinders. Each
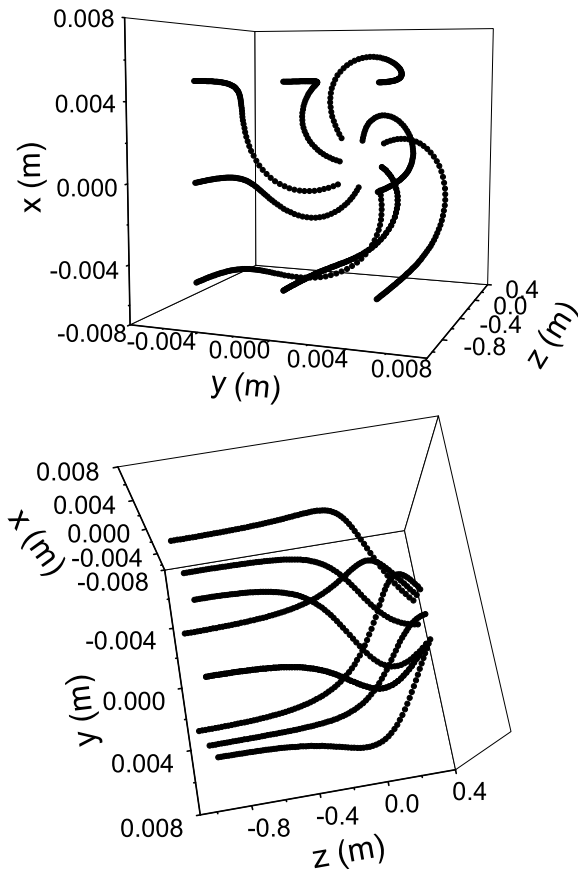
Figure 2: Two views of an incoming muon beam in an applied field of 0.45 T. The beam profile is a square of area 1 cm^2.
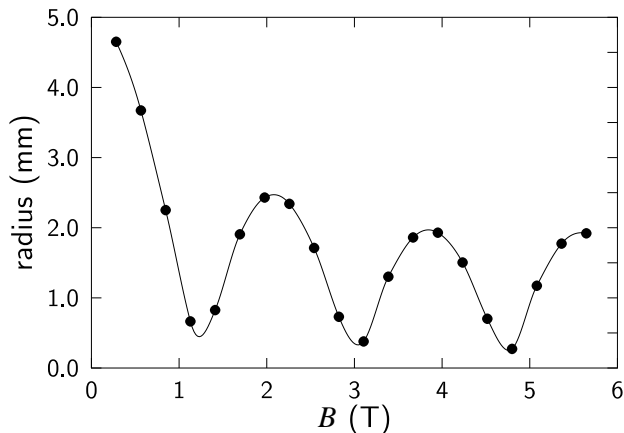
Figure 3: The radius of a collimated cylindrical muon beam (initial radius 1 cm) at the sample position as a function of applied field. The focusing effect of the field causes a periodic modulation of the spot size with B.

cylinder is segmented into 16 strips of equal area to reduce to effect of dead-time. For the purpose of the simulations, the detector thickness was chosen to be 10 mm and the detector dead time to be 10 ns. The expected range δ of a 50 MeV positron in scintillator plastic is of the order of 200 mm [7]. Over the energy range of interest, the range may be approximated as

$$\delta = \left(\frac{\xi}{\xi_{\max}} \right) \times 0.3 \text{ m}. \tag{33}$$

With such a large range, we are faced with the possibility of positrons registering with a number of detectors. A positron leaves the experiment when its z coordinate $|z| > 1$ m or for $|x|$ or $|y| > 150$ mm. This reflects the fact that a positron outside this volume will probably hit the magnet coils, cryostat or fabric of the spectrometer.

We shall be interested in estimating the background measured in a measurement. One quantity that may be readily extracted is the *integrated asymmetry*, which we define as

$$A_{\mathrm{int}} = \frac{\sum_{ij} N_{\mathrm{F},i}(t_j) - \sum_{ij} N_{\mathrm{B},i}(t_j)}{\sum_{ij} N_{\mathrm{F},i}(t_j) + \sum_{ij} N_{\mathrm{B},i}(t_j)}, \tag{34}$$

where $N_{\mathrm{F},i}(t_j)$ is the number of detected events in the ith forward detector in time bin t_j.

(a)

(b)
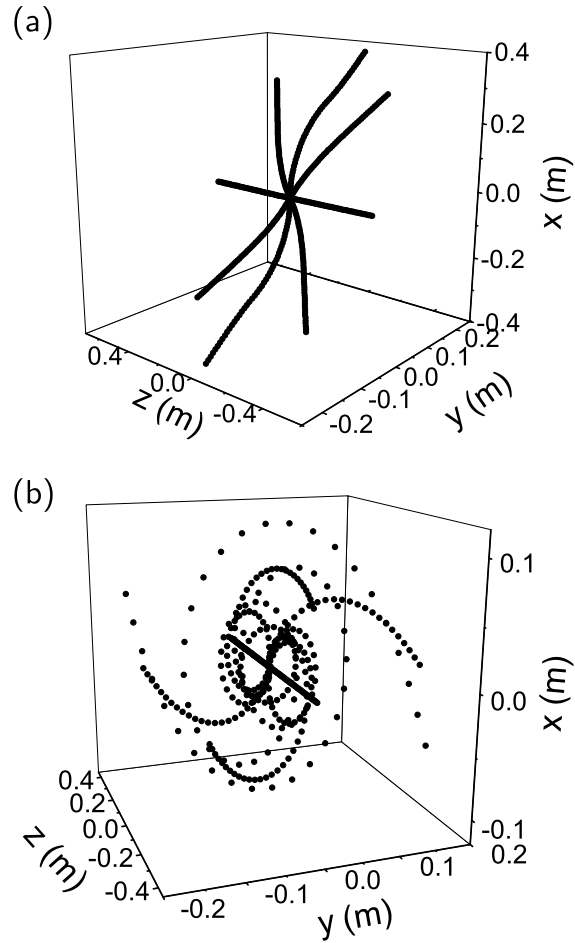
Figure 4: Positron paths for eight radially directed positrons, equally spaced in angle.(a) In an applied field of 0.45 T, the effect of the field on the trajectory is minor. (b) In an applied field of 3 T, the trajectories are significantly perturbed.
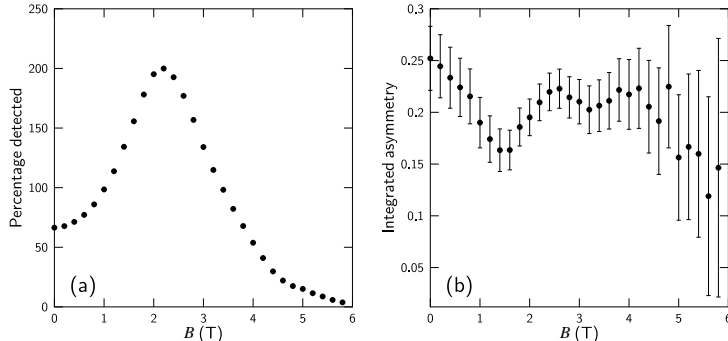
Figure 5: (a) The percentage of detected positrons as a function of applied B-field. (b) Integrated asymmetry for EMU as a function of applied B-field.

4 Results and Discussion

Despite the relativistic mechanics involved, the main principles at work in the simulation may be understood quite simply. Equation (32) shows that we would expect the radius of helical trajectories to be inversely proportional to the applied field. As the field is increased, the radius of a helical path will be reduced until it is smaller than the radius of the cylindrical detectors. At this point we would not expect a contribution in the detected data from a positron following this path. The information encoded in this positron's initial direction is therefore lost. Using equation (32) we may estimate that the cyclotron radius of a positron with the average energy will be of the order of 0.1 m in a field of order 1 T.

Figure 5(a) shows the percentage of emitted positrons detected as a function of applied magnetic field. The fact that percentages above 100% are plotted reflects the fact that a positron may make multiple hits on the detector array and therefore be detected several times. The graph is strongly peaked at $B \sim 3$ T, where the percentage rises to 200%. This corresponds to the average cylotron radius of the positrons r being comparable to the radius of the cylindrical detector arrays, leading to large numbers of multiple hits. As the field is increased, the average radius of the positron trajectories becomes smaller, causing large numbers to leave the experiment without registering on a detector.

Figure 5(b) shows the integrated asymmetry as a function of applied magnetic field (calculated for 20 pulses at each field). The interplay of effects such as the changing muon-spot size at the sample and the cyclotron-like positron paths combine to create this instrument specific background. The minimum at $B \sim 1.2$ T corresponds to the first focusing of the muon beam spot (figure 3). The large errors at high fields reflect the small number of positrons that are

detected before leaving the apparatus.

Figure 6 shows the number of positrons detected as a function of their initial energy (expressed as a percentage of the maximum positron energy). At 0 T, the distributions are those expected for positrons directed in towards the forward detectors (closed circles) or backward detectors (open circles). As the applied field is increased the contribution from low energy positrons is dramatically reduced, while that from those with energies close to the maximum is maintained. Equation (32) shows that low energy positrons will execute cyclotron orbits with smaller radii. As the field is increased, it is these positrons that will be lost from the experiment first. We see, therefore, that the applied B-field acts like an energy degrader, removing the contribution from the lowest energy (and therefore least antisymmetric) positrons. Again, we observe a peak in the number of detected events when the average cyclotron radius becomes comparable with the radius of the detector arrays.

5 Simulation of the ALC instrument

The Avoided Level Crossing (ALC) instrument [8] (figure 7) at PSI is used to measure level crossing resonances [6]. The detector and magnet geometry employed are shown in figure 8. A superconducting magnet with a 1 m long central bore, supplies fields up to 3 T. The detector geometry is, in contrast to the case of EMU, highly asymmetric. The forward detector array (through which the incoming muon beam travels) is cylindrical, while the backward detector array is a flat plate. Although the detector arrays are each split into eight sectors, the backward array uses only seven detectors, the space for the eighth being replaced with a hole through which the cryostat and sample holder protrude.

The asymmetric detector arrangements make the expected behaviour rather different to that simulated in the case of EMU. The backward detectors are not cylindrical but circular. As a result, an increasing field will cause more positrons to hit this detector array as typical cycotron radii decrease to less than the radius of the circle. We expect, therefore, that the number of events detected in the backward detectors will slowly increase with field. The more dramatic field dependent structure will be observed in the forward detector where a decrease in radius of the helical paths with increasing field will cause the number of expected events in the forward detectors to decrease as B is increased. We expect that the decrease in the number of forward events will cause the integrated asymmetry to become negative at some point.

Since PSI is a continuous muon source, the time structure of the incoming beam is very different to that considered above. The simulation does not, at this stage, include any consideration of the time structure of the PSI muon beam. For simplicity, a pulse of 1000 muons is still considered, but without the deadtime correction employed for the ISIS beam. The incoming muon beam which feeds ALC is, in reality, larger in diameter than that for EMU. It is modelled with dimensions 30×30 mm. A positron leaves the experiment when its coordinate $|z| > 1$ m or if it impinges on the superconducting magnet (i.e.
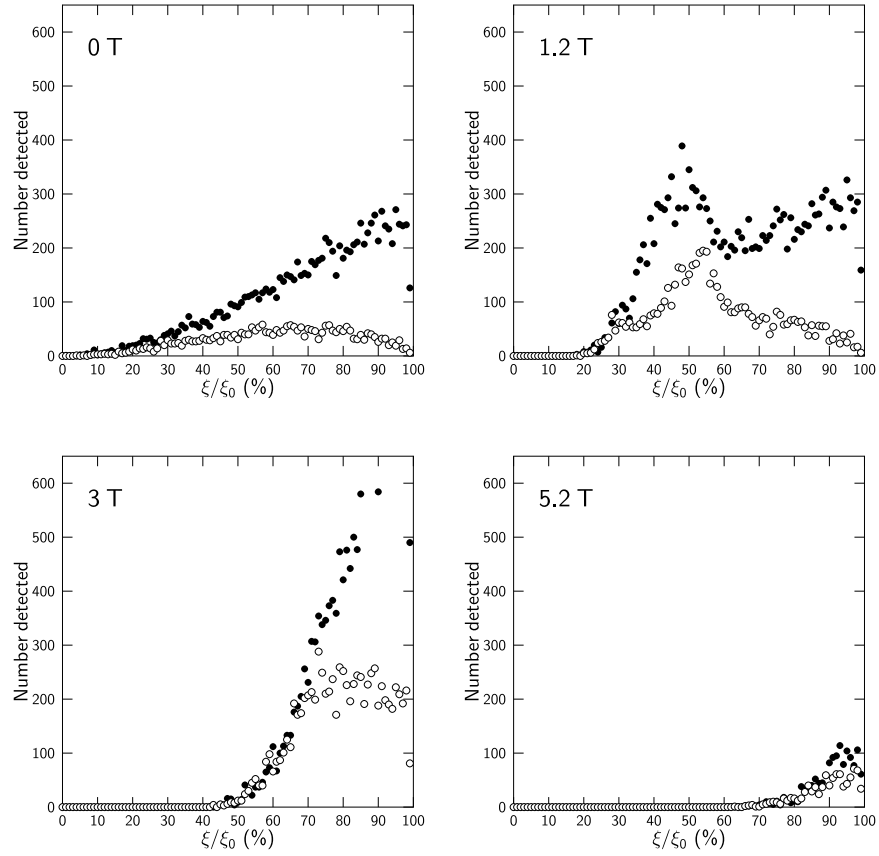
Figure 6: Number of detected positrons as a function of energy in the forward (closed circle) and backward (open circle) detector arrays. As the field is increased, lower energy positrons are not detected.

14

Figure 7: The ALC instrument at PSI, with the backward detector array and cryostat being inserted into the bore of the superconducting magnet.
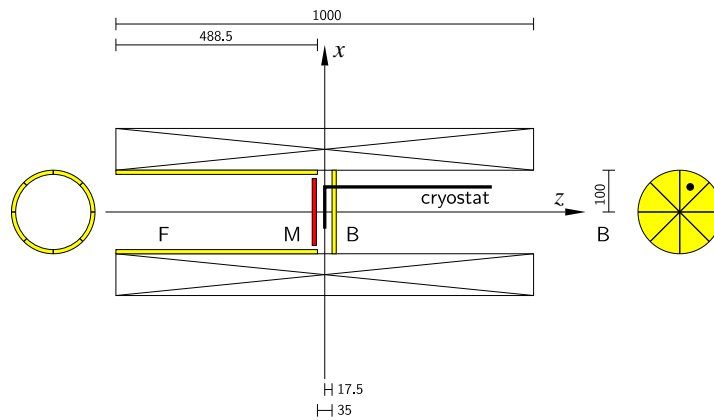
Figure 8: Schematic cross-section of the ALC spectrometer showing the superconducting magnet and detector arrays. The detector arrays are shown in yellow. The sample is located at the origin. The red detector M is the muon counter, necessary for a continuous source. All measurements are in millimetres.

when $|x|$ or $|y| > 100$ mm).

Figure 9 shows the main results of the simulation of the ALC instrument. The total number of detected positron events is shown in figure 9(a) with the counts in the forward and backward detector banks shown in figure 9(b). As predicted, the number of counts in the backward banks shows a steady increase with increasing field. The forward detectors show a large decrease in counts as the cyclotron radius becomes smaller than the radius of the cylindrical detector bank. As a result of this, the integrated asymmetry (figure 9(c)) becomes negative at around 3 T. It is not immediately clear why the number detected in the forward detector increases above 4.5 T, after an initial drop starting around 3 T. This may be due to effects related to the large size of the incoming muon beam.

We conclude that an asymmetric detector arrangement clearly has a significant effect on the instrument background. In the design of future instruments, it would be desirable to use symmetric detector banks. If an asymmetric arrangement is employed, it is important to have an accurate estimate of the background, in order that it can be distinguished from the signal due to the sample.

6   Towards a high field spectrometer

In this section we discuss the results of simulations on possible new geometries for a high field instrument at ISIS. The geometry considered is based around a proposed 7 T superconducting solenoid. The solenoid has a bore of radius 170 mm and is is split into two sections to prevent the complications related to an asymmetric detector arrangement seen in the last section. A simple detector geometry is created via cylindrical detector arrays, with radius R, separated into sixteen segments. This geometry is shown in figure 10.

Simulations have been carried out using the same incoming beam size and detector parameters as used for the EMU simulation. In this case a positrons leaves the experiment when its coordinate $|z| > 1$ m or when it impinges on the magnet (i.e. $|x|$ or $|y| > 170$ mm). The calculated integrated asymmetry and the expected numbers of events are shown for a number of detector radii R in figure 11.

For small R the number of detected events increases rapidly up to 2 T. This reflects the fact that the angular divergence of the positron ensemble at zero field causes most of the particles to miss the narrow detector bank cylinders, while the applied field causes trajectories that lie closer to the axis. This rapid increase in counts is accompanied by a pronounced minimum in integrated asymmetry near the point where the muon beam focuses for the first time. As the field increases, the number of counts goes through a broad maximum as the radii of typical trajectories and that of the detector banks become comparable. We see that at the very highest fields, the number has begun to decrease, reflecting the fact that the positron orbits will eventually become more narrow than the detector bank radius.

16
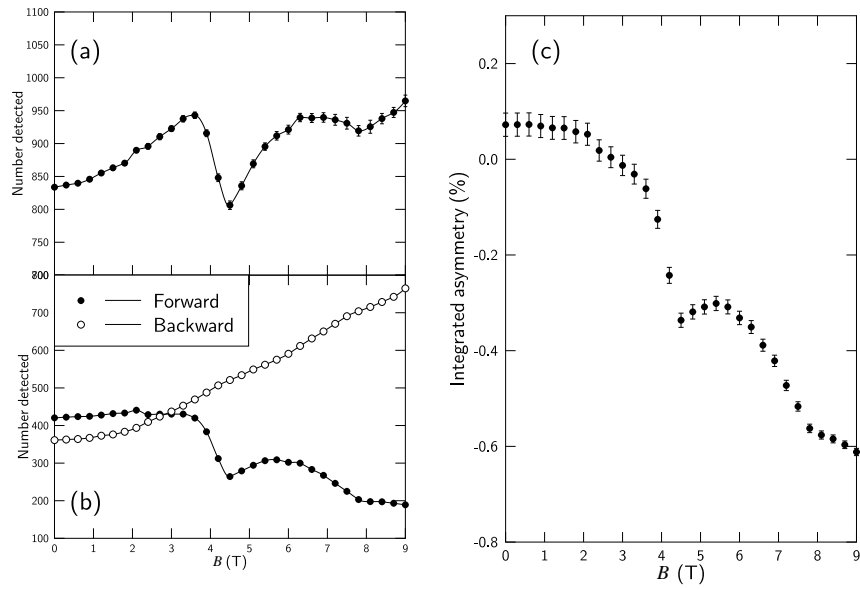
Figure 9: Main results of the simulation of the ALC spectrometer (a) The total number of positron counts as a function of applied magnetic field. (b) Number of counts in forward and backward detector banks. The most dramatic field-dependent behaviour is seen in the forward detectors. (c) The asymmetric detector geometry causes the integrated asymmetry to become negative at intermediate fields.
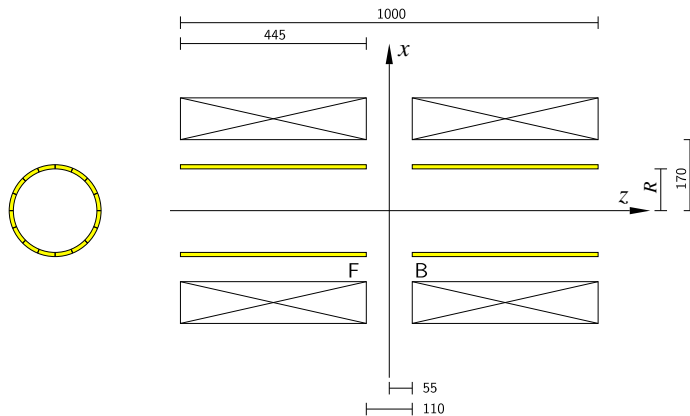
Figure 10: Schematic of the initial design of a new instrument. The field is supplied by a split superconducting solenoid. The detector array is a segmented cylinder of radius R. All measurements are given in millimetres.

For large values of R the number of detected counts quickly decreases with increasing field, falling to very low values with the application of modest magnetic fields. The structure in the asymmetry seen for small R is lost and the counting errors become very significant.

For $R = 75$ mm we obtain a compromise between the two extremes described above. The number detected goes through the expected maximum at $B \sim 2$ T, and tails off as B approaches 7 T. The structure in the asymmetry is also lost at this radius.

We also consider the distance from the $z = 0$ plane at which the positrons hit the detectors. In order to do this a new detector array is employed. This again consists of sixteen detectors in each detector bank, although now they are in the form of annular rings as shown in figure 12(a). The results of the simulation with this detector configuration is shown in figure 12(b).

For all values of R, the detector closest to the origin detects the most events. As R is increased we see that for a large applied field (where the total number of detected events is relatively low) the detectors closest to, and furthest away from, the origin detect the most events, with those in the centre of the array detecting the fewest.

We have seen that the radius of the detector arrays and their distance from the sample will need to be carefully chosen, if the proposed magnet is to be used as the basis of a high field spectrometer. It is likely that a detector geometry comprising two pairs of cylinders with different radii (as on EMU) will provide an effective solution to the problems of detector array radius dependence and minimise the effects of detector dead-time. The choice of detector arrangement will

18
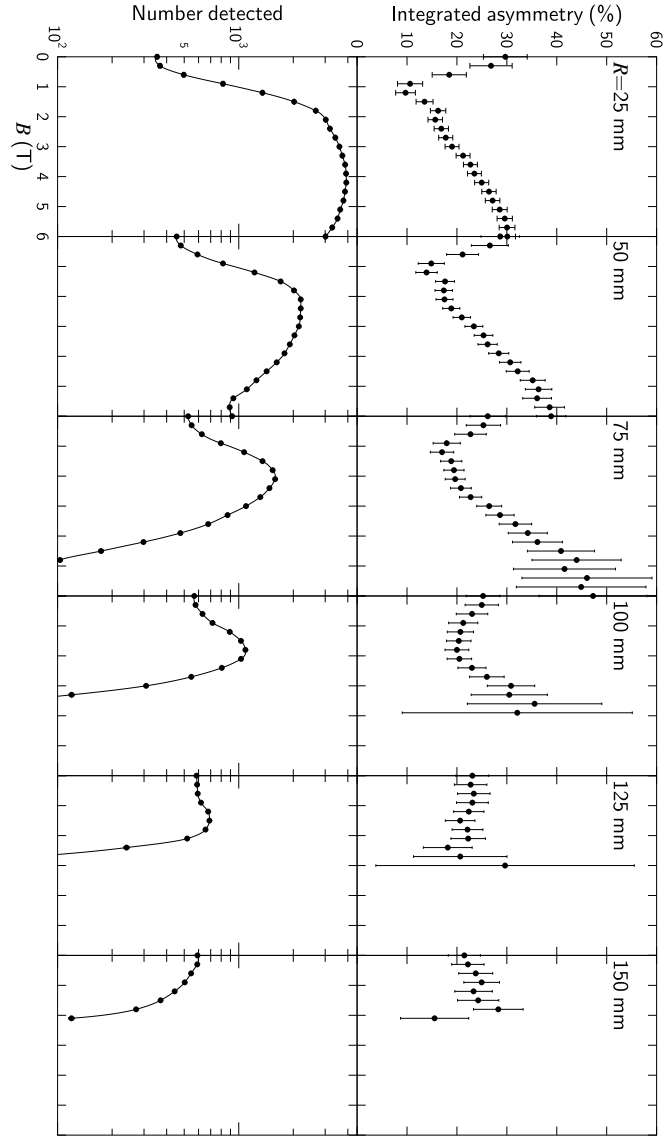
Figure 11: Results of the simulation on the new instrument geometry for several detector bank radii R. *Upper panels:* Integrated asymmetry as a function of applied magnetic field. *Lower panels:* Number of detected positron events with applied field. All x-axes are identical.
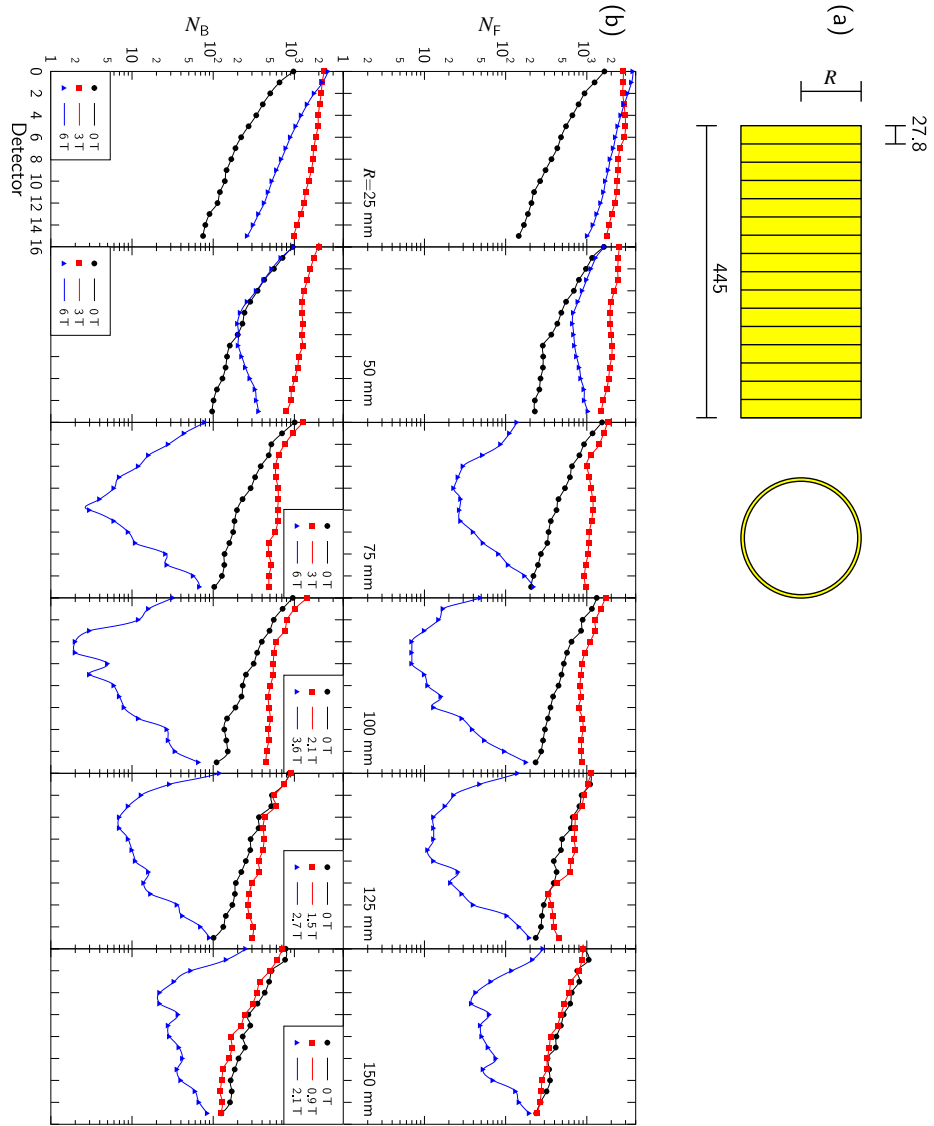
Figure 12: (a) Detector arrangement used to test the number of detected events as a function of distance from the sample (all measurements in mm). The two cylindrical detector arrays are each split into sixteen rings as shown. Detectors are numbered such that detector 1 is closest to the sample and detector 16 furthest away, for both forward and backward arrays. (b) Results of the simulation on the new instrument geometry. *Upper panels:* Number of positron counts summed over twenty runs in the forward detectors. *Lower panels:* Same as above for the backward detector banks. All x-axes are identical.

be subject to practical considerations such as the space required for photomultiplier tubes, sample environment equipment and the fabric of the spectrometer itself. Such considerations are outside the scope of the model at present. It will also be necessary to decide whether the proposed instrument is to be used exclusively at high fields, or over the entire field range.

7 Conclusion

In this paper we have discussed a first attempt at the numerical simulation of μ^+SR instruments. We have outlined the relativistic particle mechanics required to model the trajectories of charged particles in external magnetic fields and have applied this formalism to three spectrometers.

Inevitably this approach involved several approximations. Future work will involve moving towards a more realistic model of the instruments. Most significantly, the time structure of the incoming muon pulse must be included more accurately. The pulse at ISIS includes 10,000 muons stretched over 90 ns, in contrast to the zero width pulse considered here. The inclusion of the beam-line quadrupoles focusing this incoming beam is also necessary to accurately calculate the pitch of the incoming beam at the sample.

Future work will involve the integration of models such as that considered in this paper with existing beam-optics software (see, for example, [10]). The goal of such an approach will be a model of a general μ^+SR spectrometer at ISIS or PSI, which will, for example, be able to calculate effects due to sample environment equipment or the presence of degraders. This should allow a detailed understanding of spectrometers already in existence and a means of modelling those created in the future.

References

[1] King P J C, Cottrell S P, Cox S F J, Eaton G H, Hillier A D, Lord J S, Pratt F L, Lancaster T and Blundell S J 2003 *Physica B* **326** 260

[2] Bleaney B I and Bleaney B 1976 *Electricity and Magnetism* (Oxford: OUP)

[3] Landau L D and Lifshitz E M 1975 *The Classical Theory Of Fields* (Oxford: Butterworth Heinemann)

[4] Press W H, Teukolsky S A, Vetterling W T and Flannery B P 1992 *Numerical Recipes in Fortran 77: The Art of Scientific Computing (2nd ed.)* (Cambridge: CUP)

[5] http://www.isis.rl.ac.uk/muons/emu/index.htm

[6] Roduner E and Fischer H 1981 *Chem. Phys.* **54** 261

[7] *Saint-Gobain Crystals and Detectors,* http://www.bicron.com/

[8] http://lmu.web.psi.ch/facilities/alc/alc.html

[9] Roduner E 1999 in *Muon Science* (Bristol: IOP)

[10] Doornbos J, http://www.triumf.ca/people/doornbos/homepage.html